Structure analysis, tuning photoluminescence and enhancing thermal stability on Mn^{4+}-doped $La_{2-x}Y_xMgTiO_6$ red phosphor for agricultural lighting

Shujie Gai[a,b,c,1], Haifeng Zhu[a,b,1], Peixin Gao[a], Cheng Zhou[a], Zihui Kong[a], Maxim S. Molokeev[d,e], Zhiyong Qi[f,*], Zhi Zhou[a,b,**], Mao Xia[a,b,***]

[a] School of Chemistry and Materials Science, Hunan Agricultural University, Changsha, 410128, PR China
[b] Hunan Optical Agriculture Engineering Technology Research Center, Changsha, 410128, PR China
[c] College of Agronomy , Hunan Agricultural University , Changsha , 410128, PR China
[d] Laboratory of Crystal Physics, Kirensky Institute of Physics, Federal Research Center KSC SB RAS, Krasnoyarsk, 660036, Russia
[e] Siberian Federal University, Krasnoyarsk, 660041, Russia
[f] School of Architecture and Art, Central South University, Changsha, 410083, China

ABSTRACT

Currently, phosphor-converted LEDs (pc-LEDs) are revolutionizing the industry of plant growth lighting. To meet the requirements of this technology, phosphors with tunable photoluminescence, high thermal stability and luminous intensity are required. Herein, we found that the simple substitution of yttrium for lanthanum in $La_2MgTiO_6:Mn^{4+}$ (LMT:Mn^{4+}) system could satisfy above three criteria simultaneously. The photoluminescence properties can be regulated by continuously controlling the chemical composition of $La_{2-x}Y_xMgTiO_6:Mn^{4+}$ solid solution. The La sites are occupied by Y ions, causing a significant blue shift in the emission spectra which owing to the change of local crystal field strengthen. Meanwhile, the thermal stability and decay lifetimes are also varied due to the variation of local structure and band gap energy. The thermal stability of the material reaches 83.5% at 150 °C, which is better than the reported $La_2MgTiO_6:Mn^{4+}$ and $Y_2MgTiO_6:Mn^{4+}$ phosphors. The electronic luminescence (EL) of pc-LED devices using $La_{2-x}Y_xMgTiO_6:Mn^{4+}$ red phosphor is evaluated, which matching the absorption regions of plant pigments well, reflecting the superiority of the studied phosphors in plant growth lighting areas.

1. Introduction

Facility agriculture, as an effective strategy to increase the added value of agricultural products, is used worldwide with the development of modern agriculture technology [1–3]. This is because it can provide adjustable growth parameters for plant growth and development, and ensures the quality and yield of agricultural products [4,5]. Among them, supplemental light is a key technical parameter that can directly regulate plant growth and development, morphogenesis and physiological metabolism, etc., which helps to improve the growth rate of crops, accelerate the accumulation of photosynthetic products and enhance the quality of agricultural products [6,7]. Researches show that the photosynthetic pigments (including chlorophyll A, chlorophyll B, and

carotenoids) and phytochrome (including P_R and P_{FR}) are mainly absorb blue (390–500 nm), red (590–690 nm), and far-red (690–800 nm) light, which participate in regulating the entire process of photosynthesis, germination, growth and flowering in plants [8,9]. At present, the LED plant growth lamp composed of "blue light chip + red phosphors" has replaced the conventional light source and has been widely used in facility agriculture [5,10,11]. Although the commercial red phosphor (such as $Ca_{1-x-y}Sr_xBa_yAlSiN_3:Eu^{2+}$, $Ca_{2-x-y}Sr_xBa_ySi_5N_8:Eu^{2+}$ and $K_2SiF_6:Mn^{4+}$ phosphor) have superior luminous properties, their raw materials are expensive and the far-red light component is rare in their emission spectra, which make them cannot meet the light requirements of plants and has greatly limited its application in the field of agricultural lighting [12–15]. Therefore, obtain

---

a red or far-red phosphor with high luminous performance is an important and difficult problem in the research of plant supplement light.

As a tetravalent transition metal, manganese (Mn^{4+}) has a 3 d^3 electron configuration and usually exhibits red or far-red emission in fluorides and oxides [16,17]. For Mn^{4+} activated phosphors, the luminescence performance is closely related to the crystal field environment around the luminescence center. In general, Mn^{4+} prefers to occupy the octahedral lattice sites and the luminescence properties can be adjusted by changing the arrangement, distortion and tilt of the octahedral lattice [18,19]. Up to date, matrix materials with dual perovskite structures (such as La_2MgTiO_6 (LMT) [20], Y_2MgTiO_6 (YMT) [21,22], La_2CaHfO_6 [23] and La_2MgGeO_6 [24], etc.) have the advantages of good chemical stability, thermal stability, easy preparation. The abundant population of $[TiO_6]$, $[MgO_6]$, $[HfO_6]$ and $[GeO_6]$ octahedral in these phosphors provide possible occupying sites for Mn^{4+} ions. Among them, LMT:Mn^{4+} phosphor, it can be excited efficiently by a blue LED chip and exhibits red and far-red emission with emission peak at about 710 nm [20]. Similarly, the first synthesis of Mn^{4+}-doped YMT phosphor was reported in 2018, it shows a broad near UV-blue excitation band and red emission band (emission peak at 698 nm), implying a promising usage as plant-growth-lighting materials [21]. However, to further realize the application of these phosphors in plant growth lighting, the following several aspects need to be improved: improving luminous intensity, quantum efficiency and thermal stability. For LMT:Mn^{4+} phosphor, some measures have been adopted to ameliorate the luminescent properties: (i) choosing applicable flux. Liao et al. reported that LiCl could improve the thermal stability and regulate the morphology of LMT:Mn^{4+} [25]; (ii) adopting energy transfer strategy. Lin and colleagues found that co-doping with Bi^{3+} can improve the thermal stability and Internal quantum efficiency (IQE) of LMT:Mn^{4+} [20]; (iii) replacing Mg^{2+} with Zn^{2+}. Lin et al. prepared a series of $La_2Mg_{1-x}Zn_xO_6$;Mn^{4+} phosphors, but the improvement properties are unsatisfactory [20]. Despite these measures have been shown to improve the photoluminescence performance of LMT:Mn^{4+}, the strategies about tuning spectral were not reported. As for YMT:Mn^{4+} phosphor, there has been no report about its modification until now.

In general, compared with Eu^{2+}, Ce^{3+} and Mn^{2+}, the emission spectrum of Mn^{4+} is difficult to be adjusted [26,27]. This is because the $^2E{\rightarrow}^4A_2$ of Mn^{4+} belongs to the spin forbidden transition, which is manifested as line spectral emission. The peak value is usually around 690–710 nm for oxides and 630 nm for fluorides, and the transition is little affected by the crystal field [18,26]. However, in some particular lattice structure, the emission of Mn^{4+} can be changed by modulating the local crystal field strengthen of luminescence center. Based on this, some successful cases have been reported. For example, Zhou et al. reported that a 3.6 nm red shift of emission spectra was be implemented by introducing the Ge^{4+}-Li^+ to replace Al^{3+}-Ca^{2+} ion pair in $Ca_{14}Ga_{10}Zn_6O_{35}$:Mn^{4+} (CGZO:Mn^{4+}) phosphor. Meanwhile, the emission intensity, thermal stability and quantum efficiency (QE) were also significantly enhanced [28]. A red-shift was announced by replacing Ge^{4+} with Ti^{4+} ion in $Mg_{14}Ge_5O_{24}$:Mn^{4+} phosphor [29]; Similar tunable luminescence performances are also found in $(Ba_{1-x}Sr_x)_2YSbO_6$:Mn^{4+} phosphor due to the substitution of Sr^{2+} to Ba^{2+} [30]. Take inspiration from these literatures, cation substitution is a promising strategy to change the structure of the host lattice and further optimize the spectral range, thermal stability, luminous intensity and QE of phosphors. Therefore, we tried to substitute La^{3+} with Y^{3+} in LMT:Mn^{4+} phosphor to understand the effect of the change in local structure on the photoluminescence properties of phosphors during this process.

In this work, a novel Mn^{4+}-doped $La_{2-x}Y_xMgTiO_6$ red phosphor with tunable emission properties, great improved luminescent intensity, thermal stability and QE are discovered. The crystal structure, luminescence performance, QE and thermal stability of the samples were researched by combining experimental and computational methods, including Rietveld refinement, electron microscopy, spectrum and decay time measurement. Moreover, the LED devices, which combine as-prepared phosphor with the blue chips, show bright blue and red emission which match with the plant absorption spectrum well, indicating that these materials are promising candidates in indoor plant lighting.

2. Experimental section

2.1. Samples synthesis and pc-LEDs fabrication

A range of phosphors $La_{2-x}Y_xMgTiO_6$:$0.002Mn^{4+}$ (x = 0–2) were prepared through high-temperature solid-state method. Proper amounts of Y_2O_3 (99.999%, Aladdin), La_2O_3 (99.999%, Aladdin), MgO (99%, Aladdin), TiO_2 (99%, Aladdin), H_3BO_3 (99.5%, Aladdin) and $MnCO_3$ (99.999%, Aladdin) as starting materials. According to the target compounds, the materials were weighed. Particularly, 5% excess of MgO is weighted to ensure the purity of products and 2 wt% H_3BO_3 is added to promote the decomposition of carbonate. Besides, a moderate amount of alcohol was also employed to blend these powders more fully. After that, the mixtures were ground adequately for 30 min, then pre-fired at 1000 °C for 8 h at tube furnace. These precursors were reground for 20 min when the temperature of hearth is low enough. After that, these samples were sent in the same tube furnace and continued to sinter at 1350 °C for 24 h with a heating rate of 5 °C/min in the whole process. In the process, 3.0 g raw materials (Y_2O_3, La_2O_3, MgO, TiO_2, H_3BO_3, $MnCO_3$) in the given stoichiometric ratio can produce ~2.5 g products.

The pc-LED devices were manufactured by combining as-prepared red LMT:$0.002Mn^{4+}$, YMT:$0.002Mn^{4+}$ phosphor and 460 nm blue chips. The sample phosphor was blended uniformly with epoxy resin A and B (A:B = 2:1) in the agate mortar and the obtained mixture was spread on a 460 nm blue chip evenly. After that, the as-fabricated devices were transferred in an oven to solidify epoxy resin completely at 120 °C for 12 h. At last, all devices cooled down to room temperature naturally and kept in the box for characterization farther.

2.2. Sample characterizations

Powder X-ray diffraction (XRD) patterns were measured range from 10° to 80° by a diffractometer (D/SHIMADZU-6000, Japan) with Cu-Kα radiation source (λ = 1.5406 Å). The scanning rate and operating conditions was set at 6°/min and 40 kV, 40 mA. Fine structure data including lattice parameters were recorded in a step-scanning mode obtaining by a D8 Advance diffractometer (Bruker Corporation, Germany). The step size, counting time per step and measured range was set at 0.02°, 5 s and 5° to 120°, respectively. The data of LMT (JCPDS No. 70–4252) and Dy_2MgTiO_6 were adopted as the incipient model. TOPAS 4.2 software was used to conduct the XRD Rietveld refinement [31]. The micromorphologies of the samples were investigated using a double-beam scanning electron microscope (FEI helios nanolab G3 UC, USA). F-4700 fluorescence spectrophotometer (Hitachi, Japan) equip with a 150 W Xe lamp was used to obtain the PL and PLE spectra. Thermal stability was collected by a heat controller (Orient KOJI, China) in combination with F-4700 spectrophotometer. U-3310 spectrophotometer (Hitachi, Japan) was used to test the UV–vis absorption spectra. The decay times were examined by FLS920 spectrometer (Edinburgh, UK), equipped with a Xe900 lamp. QE-2100 testing system (Otsuka, Japan) was used to collect the quantum efficiency. ATA-500 measurement system (Everfine, China) was used to test the electroluminescence (EL) spectrum of LED devices.

3. Results and discussion

3.1. Structural characterization and micromorphologies

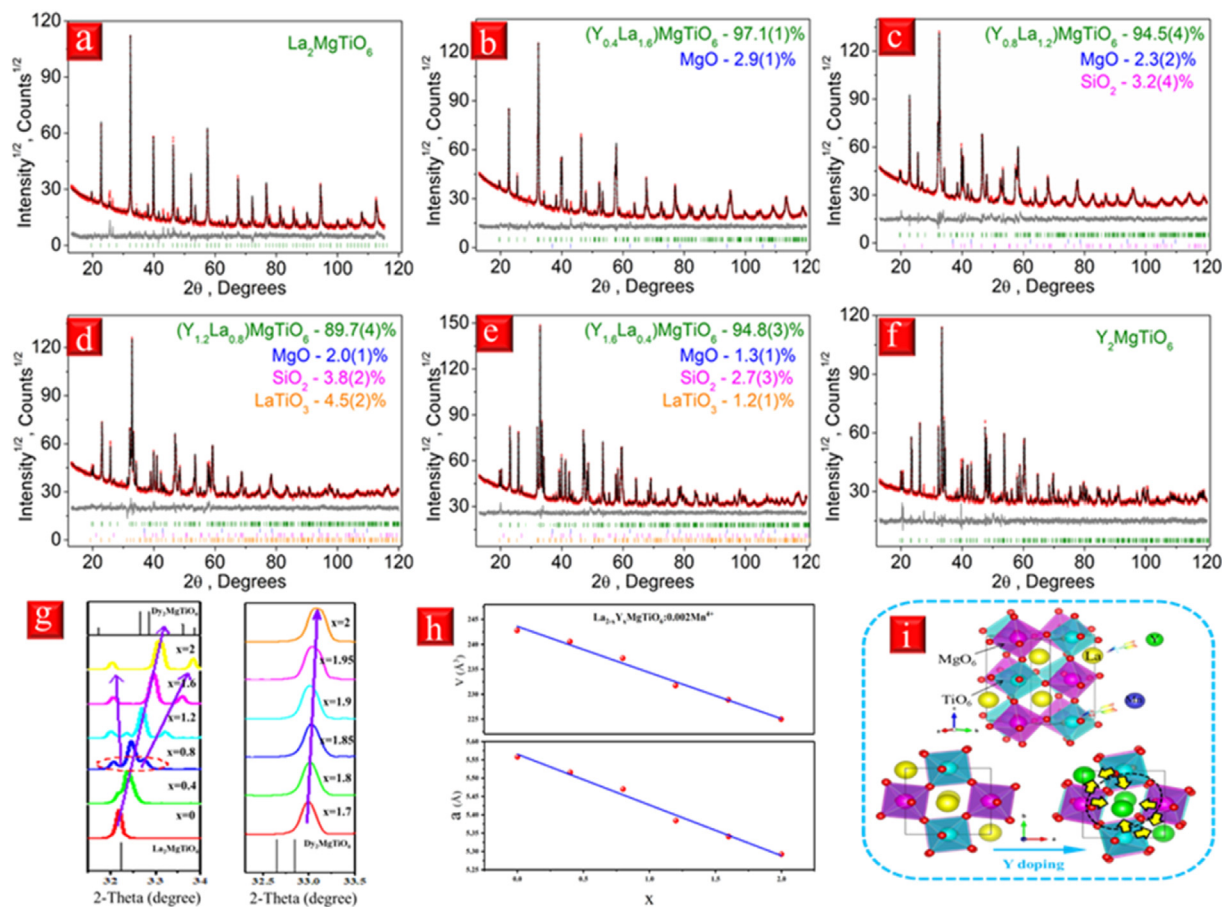For the samples with Y^{3+} incorporation, the XRD Rietveld

Fig. 1. Powder XRD Rietveld refinement patterns of $La_{2-x}Y_xMgTiO_6$: Mn^{4+}. (a) x = 0, (b) x = 0.4, (c) x = 0.8, (d) x = 1.2, (e) x = 1.6 (f) x = 2; (g) the enlarged XRD patterns of $La_{2-x}Y_xMgTiO_6$:Mn^{4+} phosphors; (h) the variations of lattice parameter versus various Y^{3+} doping content; (i) schematic illustration of the effect of Y^{3+} doping on local crystal structures.

Table 1
Crystallographic parameters obtained from XRD Rietveld refinements for $La_{2-x}Y_xMgTiO_6$:Mn^{4+} phosphors.

	x = 0	x = 0.4	x = 0.8	x = 1.2	x = 1.6	x = 2
Space group	$P2_1/n$	$P2_1/n$	$P2_1/n$	$P2_1/n$	$P2_1/n$	$P2_1/n$
a (Å)	5.5579 (9)	5.51539 (11)	5.4702 (2)	5.3841 (3)	5.34094 (7)	5.29257 (9)
b (Å)	5.5587 (4)	5.57319 (10)	5.5856 (2)	5.5822 (3)	5.58944 (7)	5.58203 (10)
c (Å)	7.8591 (7)	7.82612 (15)	7.7868 (3)	7.7107 (4)	7.66703 (10)	7.61560 (13)
V (Å^3)	242.80 (5)	240.562 (8)	237.921 (16)	231.74 (2)	228.882 (5)	224.988 (7)
β	90.015 (8)	90.021 (2)	89.912 (6)	89.898 (2)	89.8362 (9)	90.2435 (10)
R_{wp} (%)	9.59	5.26	5.96	5.18	3.91	6.05
R_p (%)	6.96	4.09	4.41	3.82	2.90	4.29
R_B (%)	5.86	2.26	1.36	1.50	0.69	1.10
χ^2	1.64	1.38	1.87	1.74	1.47	1.75

refinements of $La_{2-x}Y_xMgTiO_6$:Mn^{4+} phosphors are conducted and displayed in Fig. 1a–f. We used the data of Dy_2MgTiO_6 with alike structure as the incipient model, because the information of YMT was lacking in the inorganic crystal information database (ICSD) [21,22]. It could be found that most diffraction peaks, except several small impurity SiO_2 (usually appears after grinding), MgO and $LaTiO_3$ peaks, are indexed to the monoclinic cell ($P2_1/n$) with arguments verge on YMT. Although it is difficult to obtain a pure phase in the prepared sample, Mn^{4+}-doped impurities had no photoluminescence emission. Therefore, a small amount of impurity phase does not affect the luminescence of the main phase. The refined parameters are collected and listed in Table 1. It could be observed that all the fraction factors (R_{wp}, R_p, R_B and χ^2) converged in reasonable ranges, implying that these refinements are reliable. Other refined parameters, including coordinates of atoms and main bond lengths, are listed in Supporting Information

Tables S1 and S2. In consideration of r(La^{3+}) > r(Y^{3+}), the diffraction peaks of $La_{2-x}Y_xMgTiO_6$:Mn^{4+} shift toward larger angles as x goes up, implying a lattice shrinkage (Fig. 1g, Figs. S1 and S2). Interestingly, when $x \leq 0.4$, the diffraction peaks only move to a higher angle, while $x \geq 0.8$, a distinct phenomenon of peaks splitting and shift can be observed. According to the refinement results, the substitutions of Y^{3+} ions for La^{3+} lead to the cell volume (V) and lattice constants successive decrease, corresponding to the fact of r(La^{3+}) > r(Y^{3+}) (Fig. 1h). These results illustrate that La^{3+} sites are explicitly occupied by the Y^{3+} ions to form solid solutions. Furthermore, which will induce variation of local structural, and affect photoluminescence properties.

Based on the Rietveld refinement information, Fig. 1i displays the crystal structure of the monoclinic $La_{2-x}Y_xMgTiO_6$. They all belong to $A_2BB'O_6$ double perovskite structure with $P2_1/n$ space group. The Ti^{4+} and Mg^{2+} ions separately coordinated with six oxygen atoms to form
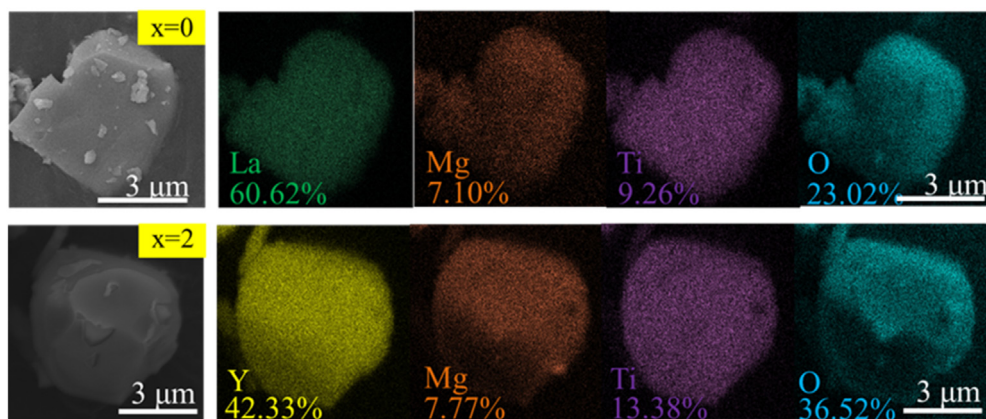
Fig. 2. SEM images and elemental mapping of two characteristic particles of LMT:Mn^{4+} and YMT:Mn^{4+} phosphor.

the twisted and tilted [TiO$_6$] and [MgO$_6$] octahedron. They are cross-linked each other by sharing O^{2-} ion in the corner, alternative arranged in two alternating face center cubic sublattices. Besides, the La^{3+}/Y^{3+} ions are occupied in the vacancies between octahedrons. The corresponding [LaO$_{12}$] polyhedron would shrink and further affect the nearby octahedral environment when the substitutions of Y^{3+} for La^{3+}. From the effective ionic radius viewpoint, the dopant Mn^{4+} (CN = 6, r = 0.53 Å) are more similar to the Ti^{4+} (CN = 6, r = 0.60 Å). Moreover, the formation energy of Mn–Ti substitution is smaller than that of Mn–Mg, according to the research of Zhou et al. [32]. Thus, these conditions make it reasonable to believe that Mn^{4+} preferentially replaces the crystallographic sites of Ti^{4+} in La$_{2-x}$Y$_x$MgTiO$_6$.

The SEM images of sample phosphor were shown in Fig. 2 and Fig. S3. Like most phosphors synthesized by high-temperature solid-state reactions, these particles show irregular shapes with constituted by agglomerated crystals. The average diameter of particles was estimated in the range of 5–10 μm, which is in agreement with the previous literatures [20,22]. Furthermore, the EDS mapping of a single particle indicates a uniform distribution of La, Y, Mg, Ti and O across the particle. However, the EDS mapping of Mn cannot be detected due to the low doping level. Particularly, the above results analysis was similar to the stoichiometric contents of the target except that the proportion of Mg is a little high, which could be attributed to the addition of additional MgO during the preparation process. These results indicate that the ideal phosphors La$_{2-x}$Y$_x$MgTiO$_6$:Mn^{4+} were successfully synthesized by solid-solution methods.

3.2. Luminescence performance of La$_{2-x}$Y$_x$MgTiO$_6$:Mn^{4+} phosphors

Fig. 3a–b records the PLE and PL spectra of LMT:Mn^{4+} and YMT:Mn^{4+} phosphors at room temperature. Two typical excitation bands are observed by monitoring at optimal emission wavelength. These excitation spectra could be well decomposed into four sub-bands by Gaussian fitting, and are assigned to Mn^{4+} → O^{2-} charge transfer (CT) transition, spin-allowed ^{4}A$_2$ → ^{4}T$_1$, spin-forbidden ^{4}A$_2$ → ^{2}T$_2$ and spin-allowed ^{4}A$_2$ → ^{4}T$_2$ transitions of Mn^{4+}, respectively [20,21,28]. In addition, some peak positions are found to be different between LMT:Mn^{4+} and YMT:Mn^{4+}, reflecting that Mn^{4+} ions are in different crystal field environment. To understand this in more detail, a series of La$_{2-x}$Y$_x$MgTiO$_6$:Mn^{4+} phosphors are prepared and measured. Fig. 3c shows the UV–vis absorption spectra of La$_{2-x}$Y$_x$MgTiO$_6$:Mn^{4+} (x = 0, 0.4, 0.8, 1.2, 1.6, 2) phosphors. Three correlative absorption bands ranging from 200 to 330 nm, 330 to 420 nm and 420 to 600 nm are observed for all samples, which could be attributed to host absorption, Mn^{4+} → O^{2-} charge transfer (CT) transition, the ^{4}A$_2$ → ^{4}T$_1$, ^{4}A$_2$ → ^{2}T$_1$ and ^{4}A$_2$ → ^{4}T$_2$ transition of Mn^{4+}, respectively [21]. This result is well-consistent to the PLE spectra. In order to obtain more information about band structures, the optical band gaps are calculated according to the

following equation [5]:

$$(\alpha h\nu)^n = A(h\nu - E_g) \tag{1}$$

where α, $h\nu$ and A represent the absorption coefficient, the photon energy and constant, respectively. E_g is the optical band gap value. According to previous report, the value of n is 1/2 since the band structures of LMT and YMT compound are indirect [20,21]. The band gap values for the La$_{2-x}$Y$_x$MgTiO$_6$:Mn^{4+} (x = 0, 0.4, 0.8, 1.2, 1.6, 2) are calculated to be 3.125, 3.024, 2.915, 3.061, 3.162, 3.509 eV, respectively (see Fig. 3d).

As displayed in Fig. 4a, with the increase proportion of Y^{3+}, the shape of the excitation spectrum is similar and the excited intensity increases at first and decreases after reaching the maxima. It could be obviously observed that the optimal x should be 1.95 in this study. The emission spectra of La$_{2-x}$Y$_x$MgTiO$_6$:Mn^{4+} phosphors upon the excitation of 350 nm are shown in Fig. 4b, it shows similar trends to the excitation spectrum. The optimal luminous performance is obtained when x = 1.95, and its intensity is 207.1% of LMT:Mn^{4+} and 102.6% of YMT:Mn^{4+}, respectively. In addition, the emission spectra gradually blue-shift with a wavelength interval of 11 nm during this process. Moreover, the change in peak shape is also particularly noticeable. Firstly, the number of emission peaks gradually decreased from four (x = 0) to one (x = 1.2), and then increased to three (x = 2). Secondly, the strongest emission peak for La$_{2-x}$Y$_x$MgTiO$_6$:Mn^{4+} show a blue-shift until x = 0.8 (692.6 nm), which is shorter than the emission peak of YMT:Mn^{4+} (699.8 nm), and then, the strongest emission peak shifted toward longer wavelengths at higher x values (see Fig. S4). The more information about luminescence spectra are listed in Table S3. It is well-known that the spectral properties of Mn^{4+} ions are nearly related to the surrounding environment of octahedron. In order to further explain the blue shift observed above, the crystal splitting field energy (D_q) and Racah parameters (B, C) were calculated according to following formulas [33,34]:

$$D_q = \frac{E(^4A_{2g} \rightarrow ^4T_{2g})}{10} \tag{2}$$

where the energy gap between ^{4}A$_2$ → ^{4}T$_2$ transition could be ascertained by the position of peaks. In addition, the value of B could be calculated on the basis of the energy difference between ^{4}A$_2$ → ^{4}T$_2$ and ^{4}A$_2$ → ^{4}T$_1$ transitions [33,34]:

$$\frac{D_q}{B} = \frac{15(\alpha - 8)}{(\alpha^2 - 10\alpha)} \tag{3}$$

where α is expressed as [33,34]:

$$\alpha = \frac{E(^4A_{2g} \rightarrow ^4T_{1g}) - E(^4A_{2g} \rightarrow ^4T_{2g})}{D_q} \tag{4}$$

By estimating the peak energy of ^{2}E → ^{4}A$_2$ transition, the values of
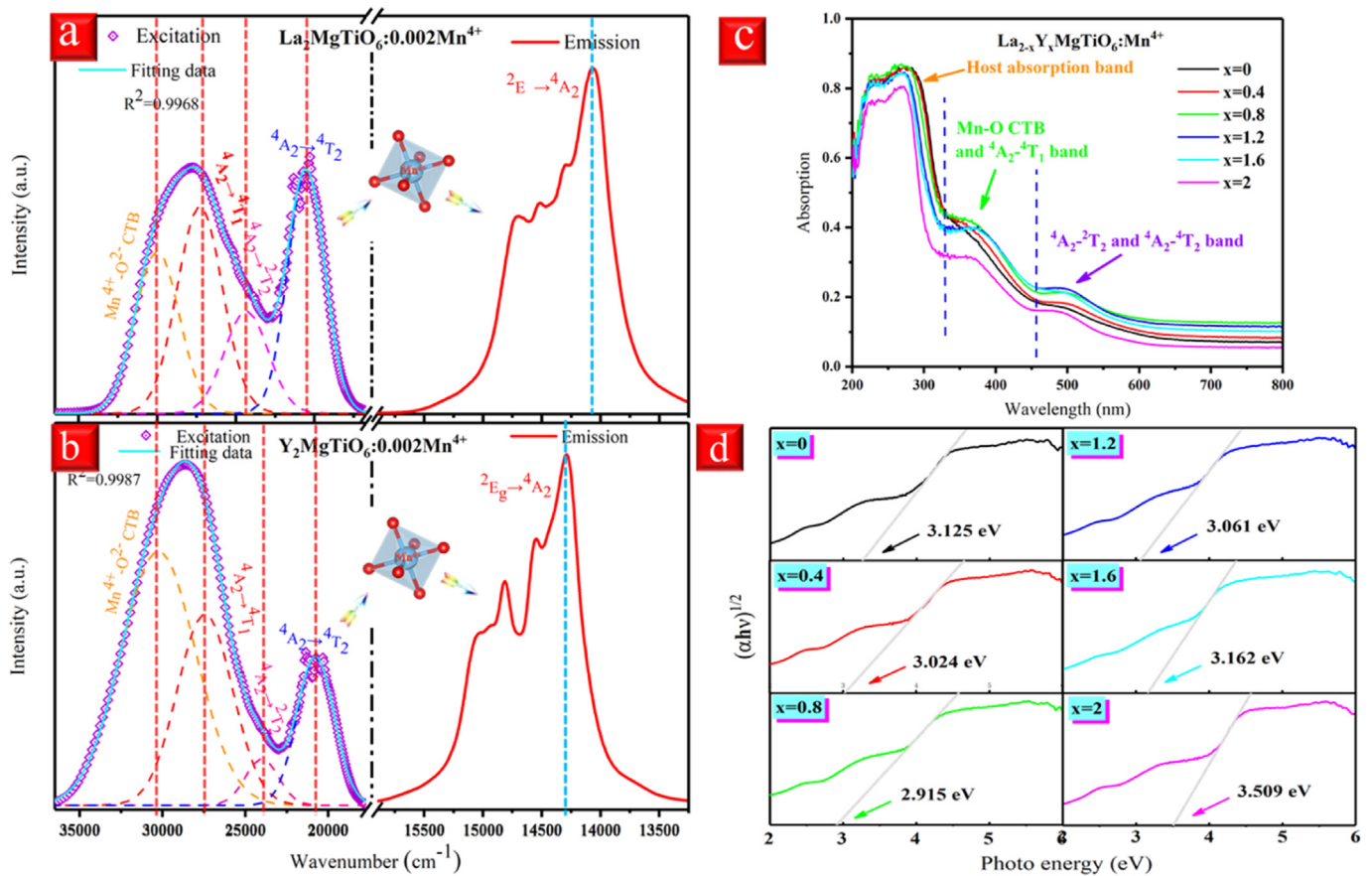
Fig. 3. Multi-peaks Gaussian fitting of the excitation spectrum of (a) LMT:Mn^{4+} and (b) YMT:Mn^{4+} phosphors; (c) the UV–vis absorption spectra of La$_{2-x}$Y$_x$MgTiO$_6$:Mn^{4+} (x = 0, 0.4, 0.8, 1.2, 1.6, 2) phosphors; (d) the fitting of corresponding band gap energies.

parameters C could be calculated as follow [33,34]:

$$\frac{E(^2E_g \rightarrow {}^4A_{2g})}{B} = \frac{3.05C}{B} - \frac{1.8B}{D_q} + 7.9 \tag{5}$$

Thus, according to equations (2)–(5), the values of D_q, B, C and D_q/B of La$_{2-x}$Y$_x$MgTiO$_6$:Mn^{4+} phosphors could be calculated and the related data were shown in Table 2. Tanabe-sugano (T-S) energy level diagram is a common method to explain the luminescence mechanism of Mn^{4+} doped phosphors, which is presented in Fig. 4c. It is worth noting that the most energy levels are affected by the crystal field strength except ^{2}E and ^{2}T$_1$ energy levels. Besides, it can conclude that the Mn^{4+} ions are exposed to a strong crystal field in the La$_{2-x}$Y$_x$MgTiO$_6$ host since the D_q/B value exceeds 2.2. In addition, it should be pointed out that the crystal field splitting gradually increased as the proportion of Y^{3+} increases, which would cause the ascended ^{2}E level and further result in the blue shift in emission spectrum of La$_{2-x}$Y$_x$MgTiO$_6$:Mn^{4+} phosphors. However, this blue shift is small (around 11 nm) due to the ^{2}E and ^{4}A$_2$ energy levels of Mn^{4+} are almost parallel. Fig. 4d displays the contrastive photos and CIE chromaticity coordinates diagram of samples under daylight and 365 nm UV lamp, implying that these are fine red glowing materials.

3.3. Temperature-dependent luminescence and decay lifetimes of La$_{2-x}$Y$_x$MgTiO$_6$:Mn^{4+} phosphors

It is necessary to measure the luminous performance of phosphor at high temperature, because the temperature of LED devices will reach about 150 °C when working. Thus, the temperature-dependent luminescence of La$_{2-x}$Y$_x$MgTiO$_6$:Mn^{4+} phosphors are measured and collected, as shown in Fig. 5a–e and Fig. S5. Clearly, the emission intensity

decreases as the temperature increases in these samples. In addition, these peaks shape and position remain almost unchanged at different temperature. Interestingly, the anti-Stokes emission intensity (620–680 nm) of La$_{2-x}$Y$_x$MgTiO$_6$:Mn^{4+} (x = 1.6–2) increases first and then decreases as the temperature increases. The reason is that the anti-Stokes sideband (upper levels) can be thermally depopulated from the Stokes sideband (lower levels) to reach thermal equilibrium when the temperature increases [21]. Furthermore, the thermal stability (T) are evaluated using the following equation:

$$T = \frac{\int_a^b I_1(x)dx}{\int_a^b I_0(x)dx} * 100\% \tag{6}$$

Where I_0, I_1 are the luminescence intensity of phosphors at normal temperature and test temperature, respectively. The corresponding experimental results are shown in Fig. 5f. In general, at 150 °C, the thermal stability of La$_{2-x}$Y$_x$MgTiO$_6$:Mn^{4+} decreases from 56.9% of LMT:Mn^{4+} to 50.3% then increase to 83.5% final decreases to 79% of YMT:Mn^{4+}, which indicating the modulation of Y^{3+} in crystal structure can improve the thermal stability of La$_{2-x}$Y$_x$MgTiO$_6$:Mn^{4+}. To better explain the thermal stability mechanism of above samples, the local structures diagram of solid solution as shown in Fig. 6. During the substitution process, the overall contraction and the local expansion (contraction) of the cell have a competitive (synergetic) relationship, affecting the local [Mg/TiO$_6$] octahedron. The substitution process could be divided into three parts. In the first part, when the small amount of Y^{3+} was added, the surrounding [Mg/TiO$_6$] octahedron would expand due to the relatively smaller ionic radius of Y^{3+}. In this process, the influence of overall contraction is less than local expansion. If Mn^{4+} occupied Ti^{4+} of these inflated octahedrons, the Mn–O bond length is bound to be longer. Longer Mn–O bond length implies that its
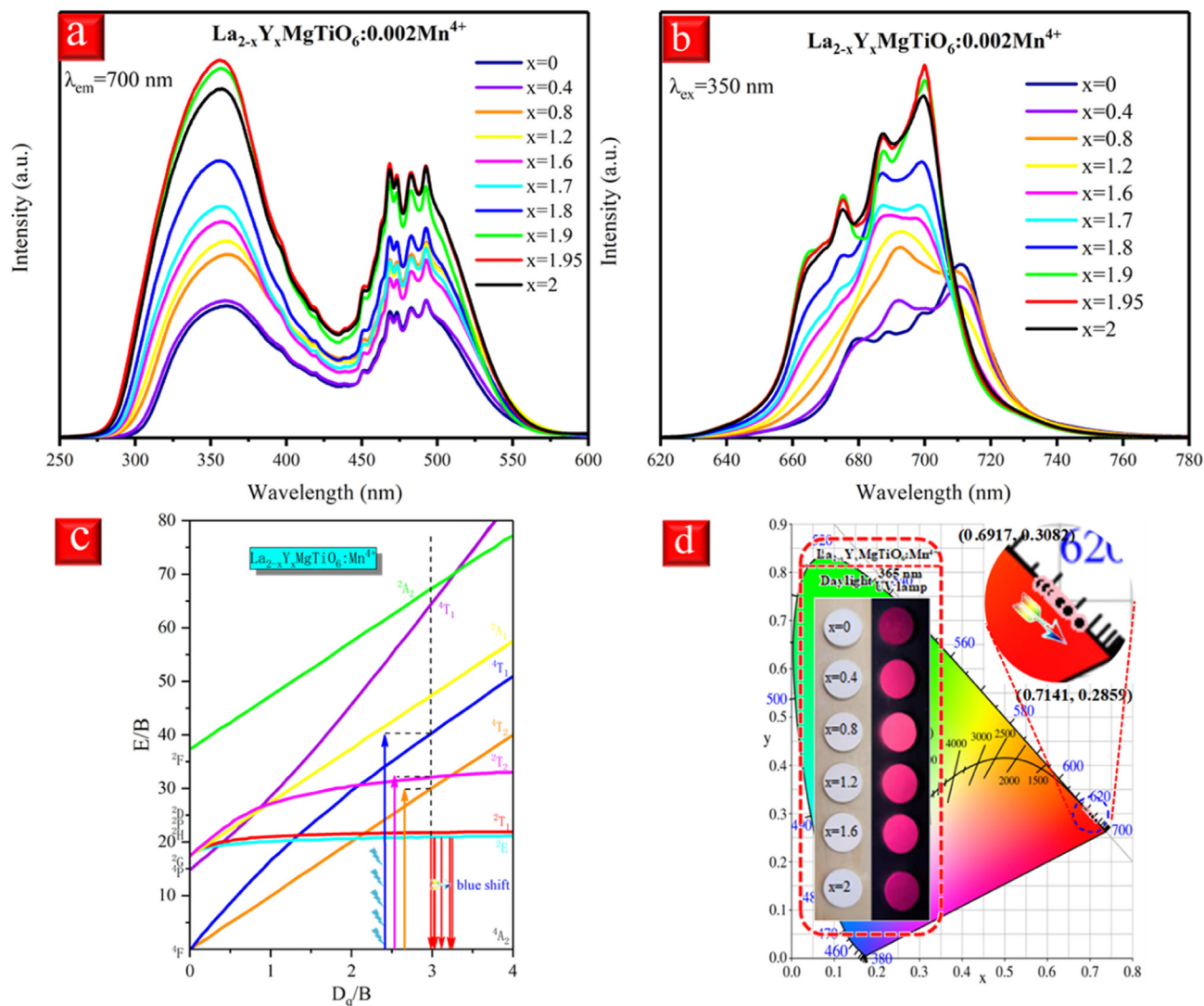
Fig. 4. (a) PLE and (b) PL spectra of La$_{2-x}$Y$_x$MgTiO$_6$:Mn^{4+} phosphors; (c) the Tanabe–Sugano energy level diagram for d^3 electron configuration in octahedron coordination; (d) CIE chromaticity diagram of La$_{2-x}$Y$_x$MgTiO$_6$:Mn^{4+} phosphors, the inset displayed the above phosphors under daylight and 365 nm UV lamp.

Dq is smaller, which would lead to the lowered ^{4}T$_2$ energy level (blue line) because 10Dq and energy level of Mn^{4+} (^{4}T$_2$) are positively correlated. Eventually which increase the non-radiation transition, resulting in the attenuated thermal stability in La$_{2-x}$Y$_x$MgTiO$_6$:Mn^{4+}. In the second part, the overall shrinkage would be more advantageous than local expansion when x continued to increase, resulting in shorter Mn–O bond length and higher ^{4}T$_2$ energy level (red line). Besides, local expansion will gradually turn into local contraction when the ratio of Y^{3+} is greater than La^{3+}. The ^{4}T$_2$ energy level is further elevated under the synergy of overall and local contraction, resulting in the increased thermal stability. In the third part, the crystal lattice continues to shrink as Y^{3+} to be added constantly. However, the position of local

contraction is reduced during this process, which lessens the effect of local shrinkage and thus reduces thermal stability.

Fig. 7a–b presents the decay curves of La$_{2-x}$Y$_x$MgTiO$_6$:Mn^{4+} excited at 350 nm and monitored at their optimal emission wavelengths. All of these curves could be well-fitted via single-exponential decay model, its expressed as follow [35]:

$$I_t = I_0 + Aexp\left(\frac{-t}{\tau}\right) \tag{7}$$

where I_t and I_0 are the luminescence intensity at time t and time 0, A refer to a constant and τ stand for the exponential component of the decay time. The calculated lifetime of La$_{2-x}$Y$_x$MgTiO$_6$:Mn^{4+} is a single

Table 2
Energy states and crystal field parameters in La$_{2-x}$Y$_x$MgTiO$_6$:Mn^{4+} phosphors.

x	E ($^4A_{2g} \rightarrow {}^4T_{1g}$) (cm-1)	E ($^4A_{2g} \rightarrow {}^4T_{2g}$) (cm-1)	E ($^2E_g \rightarrow {}^4A_{2g}$) (cm-1)	Dq	B	C	Dq/B
x = 0	27413	20353	14084	2035.3	678.4	2994.1	3.00
x = 0.4	27368	20379	14084	2037.9	669.8	3133.0	3.04
x = 0.8	27491	20471	14450	2047.1	672.8	3005.8	3.04
x = 1.2	27375	20493	14409	2049.3	656.5	3148.0	3.12
x = 1.6	27144	20513	14347	2051.3	627.5	3191.9	3.26
x = 2	27346	20700	14306	2070	628.1	3176.2	3.30

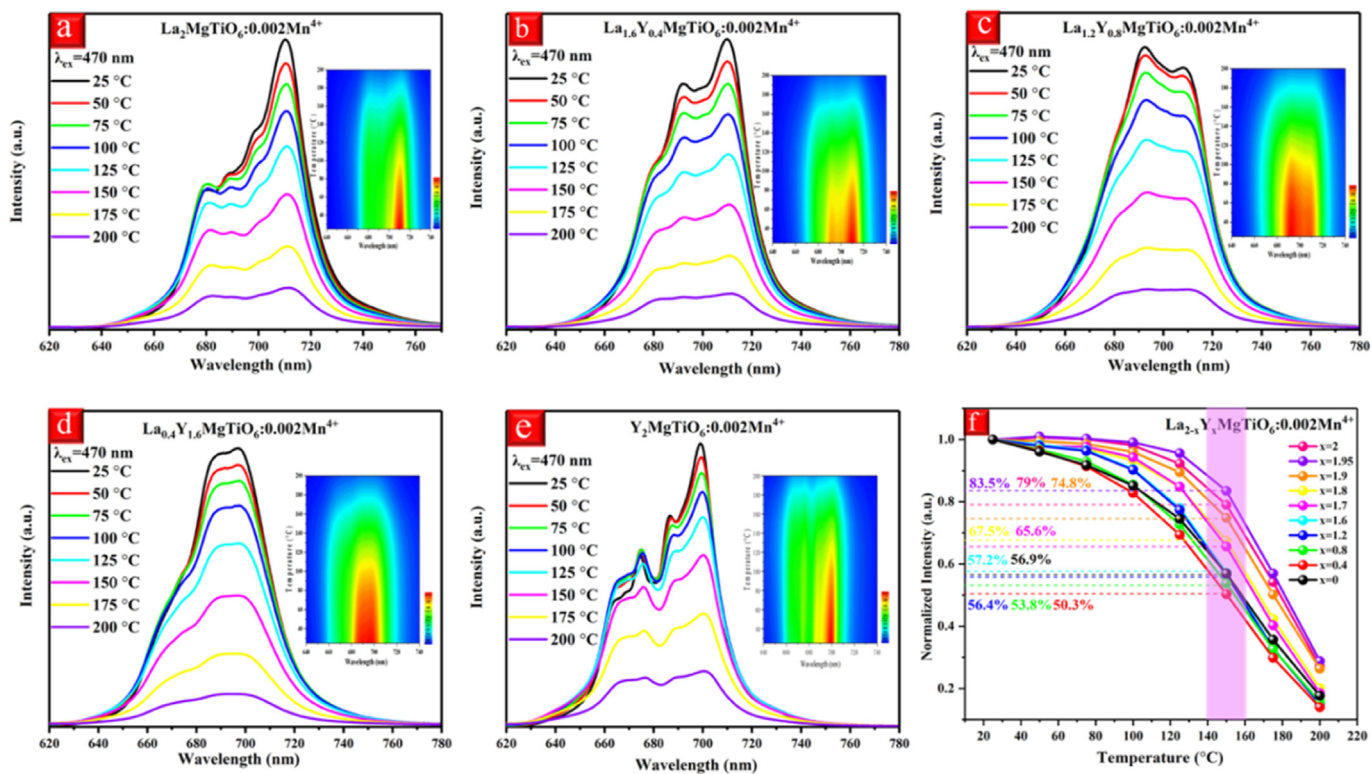**Fig. 5.** The temperature-dependent emission spectra of $La_{2-x}Y_xMgTiO_6$:Mn^{4+} phosphors. (a) x = 0, (b) x = 0.4, (c) x = 0.8, (d) x = 1.6, (e) x = 2.0; (f) the variations of normalized integrated intensities of above phosphors as functions of temperature.

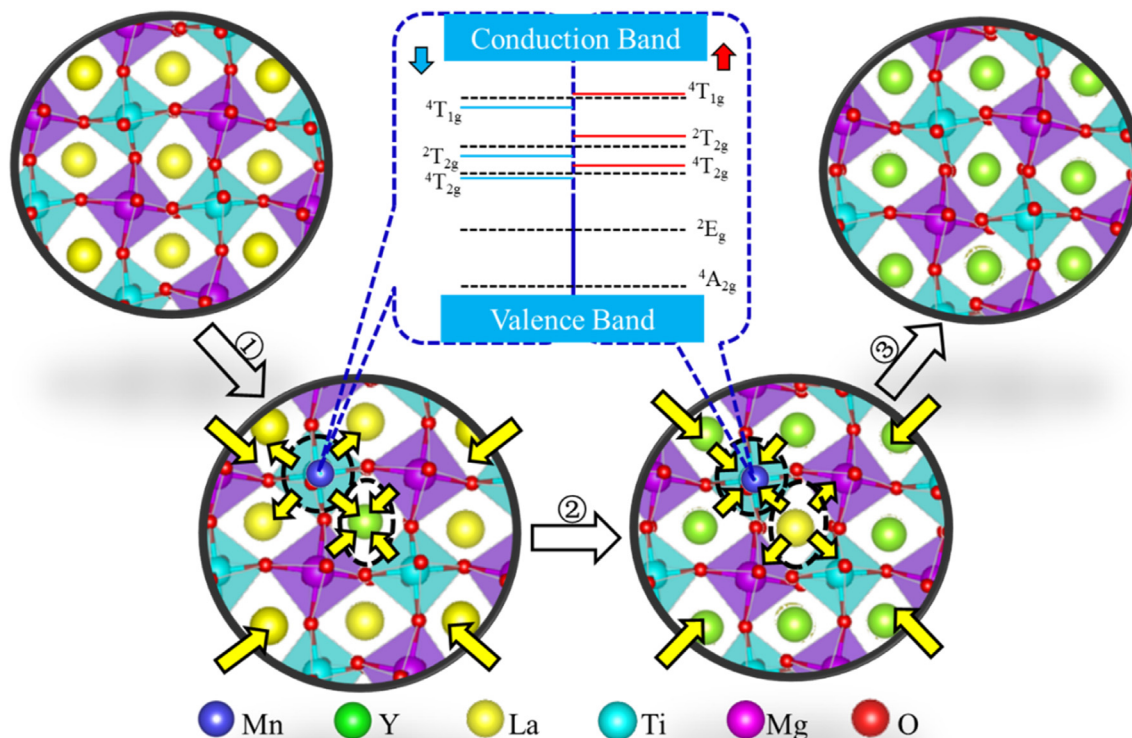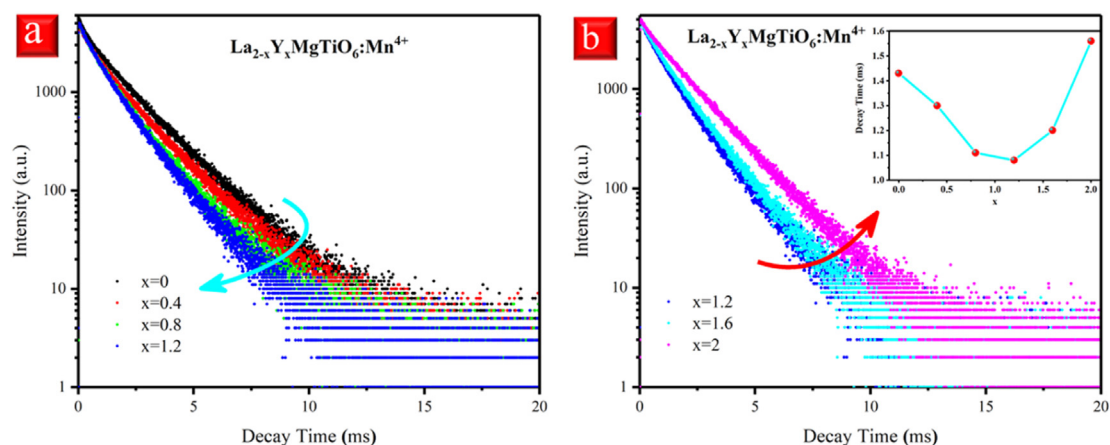**Fig. 6.** Schematic illustration of the effect of Y^{3+} doping on energy level structure of Mn^{4+}.

Fig. 7. (a)–(b) The decay times of $La_{2-x}Y_xMgTiO_6:Mn^{4+}$ phosphors upon the excitation of 350 nm and monitored at 700 nm.

exponential verified that the single Mn^{4+} emission center at Ti^{4+} site, which is in consistent with the analysis of the crystal structure. Notably, the PL lifetime decreased at first with the addition of Y^{3+} and then increased with the continuous addition of Y^{3+}. The above variation of decay lifetimes are possibly attributed to the change of band gap. The decrease of the band gap will easily decrease the difference in energy between the lowest $^4A_2$ state and the conduction band, and cause thermal-associated ionization, which is the so-call photoionization process [36]. Normally, as the band gap decreases, the luminous life-time shortens due to the extra contribution of non-radiation in decay process [37]. According to the previous results, the trend of band gap values is roughly consistent with the regular pattern of decay lifetimes. Therefore, the band gap seems to play a major role in causing this variation.

QE is a key parameter in the practical application of phosphors. Keeping this in mind, the IQE and EQE of LMT:Mn^{4+} are measured to be 32.5% and 22.2%, respectively, which are similar to Lin's report [20]. Obviously, these values enhanced to 56.7% and 42.5% after Y^{3+} doped. Table 3 and Table S4 respectively lists some Mn^{4+} doped La $(Y)_2MgTiO_6$-based phosphors and other double perovskite-type phosphors until now. It is found that the as-prepared samples show superior thermal stability and IQE value, indicating that these materials have wider applications [38–40].

3.4. Application of $La_{2-x}Y_xMgTiO_6:Mn^{4+}$ in agriculture lighting

According to the above discussion, $La_{2-x}Y_xMgTiO_6:Mn^{4+}$ phosphors have red emission and excellent thermal stability performance. Therefore, it is very significant to investigate their potential application in agriculture lighting. Based on this case, we chose LMT:Mn^{4+} and YMT:Mn^{4+} phosphors as examples to fabricate the LEDs. The devices were obtained by the combination of blue chips with above phosphors. Fig. 8a–b shows the corresponding EL spectra of LMT:Mn^{4+} and YMT:Mn^{4+} phosphor LED devices, respectively. The spectra imply that

the deep-red-light component increases obviously when the weight ratio of phosphor to resin increases from 0.5:1 to 2:1, as shown the insets in Fig. 8a–b, the light emitted by LED devices changed from blue to purple. It is well known that plants will grow faster if the light meets the requirements of plant absorption. Thus, the EL spectra of as-prepared LEDs are detailed compared with the absorption band of plant pigments. It can be clearly seen that the EL spectra of these LEDs overlap obviously with the absorption spectra of plant pigments. In briefly, by choosing different kinds of $La_{2-x}Y_xMgTiO_6:Mn^{4+}$ phosphors or adjusting the dosage of phosphors could meet the demands of different plants for light at various growth stages. The CIE chromaticity coordinates of these devices are shown in Fig. 8c. As to LMT:Mn^{4+}, it changed from (0.1438, 0.0404) of LED1 to (0.1829, 0.0846) of LED4. Similarly, for YMT:Mn^{4+}, it transfers from (0.1478, 0.0405) of LED5 to (0.1973, 0.0693) of LED8. All this reveals an important phenomenon that the increased red component. In order to further investigate the stability of as-fabricated LEDs under different driven current, the EL spectra of LED4 and LED8 were measured under different driven current from 20 to 200 mA (see Fig. 8d). It can be clearly seen that the CIE chromaticity coordinates changed from (0.1829, 0.0846) to (0.1602, 0.0861) of LED4 and (0.1973, 0.0693) to (0.1928, 0.0771) of LED8. The slight change of CIE chromaticity coordinates testifying that as-prepared devices are less affected by driven current. However, LED fabricated from YMT:Mn^{4+} has better stability at high input power compared with LMT:Mn^{4+}. All in all, the LED devices display the excellent EL properties, and their EL spectrum matches well with the absorption band of plant pigment, indicates the $La_{2-x}Y_xMgTiO_6:Mn^{4+}$ phosphors have a potential value in agriculture lighting.

4. Conclusion

In this work, the new double perovskite type solid solution phosphors of $La_{2-x}Y_xMgTiO_6:0.002Mn^{4+}$ with controllable luminescence performance were designed and prepared. The analysis of XRD

Table 3

Emission wavelengths, thermal stability and internal quantum efficiency of Mn^{4+} doped La(Y)$_2MgTiO_6$-based phosphors.

Phosphor composition	λ_{em} (nm)	Thermal stability[a] (%)	IQE (%)	Ref.
$La_2MgTiO_6:Mn^{4+}$ (LiCl)	705	47	–	25
$La_2MgTiO_6:Mn^{4+},Bi^{3+}$	710	78	59.5	20
$La_2MgTiO_6:Mn^{4+}$	710	–	31.5	20
$Y_2MgTiO_6:Mn^{4+}$	698	–	–	21
$La_2MgTiO_6:Mn^{4+}$	710.8	56.9	32.5	This work
$La_{1.2}Y_{0.8}MgTiO_6:Mn^{4+}$	692.6	53.8	40.1	This work
$La_{0.05}Y_{1.95}MgTiO_6:Mn^{4+}$	699.8	83.5	56.7	This work
$Y_2MgTiO_6:Mn^{4+}$	699.8	79	55.1	This work

[a] The thermal stability refers to the retention rate of luminescence intensity at 150 °C relative to normal temperature.
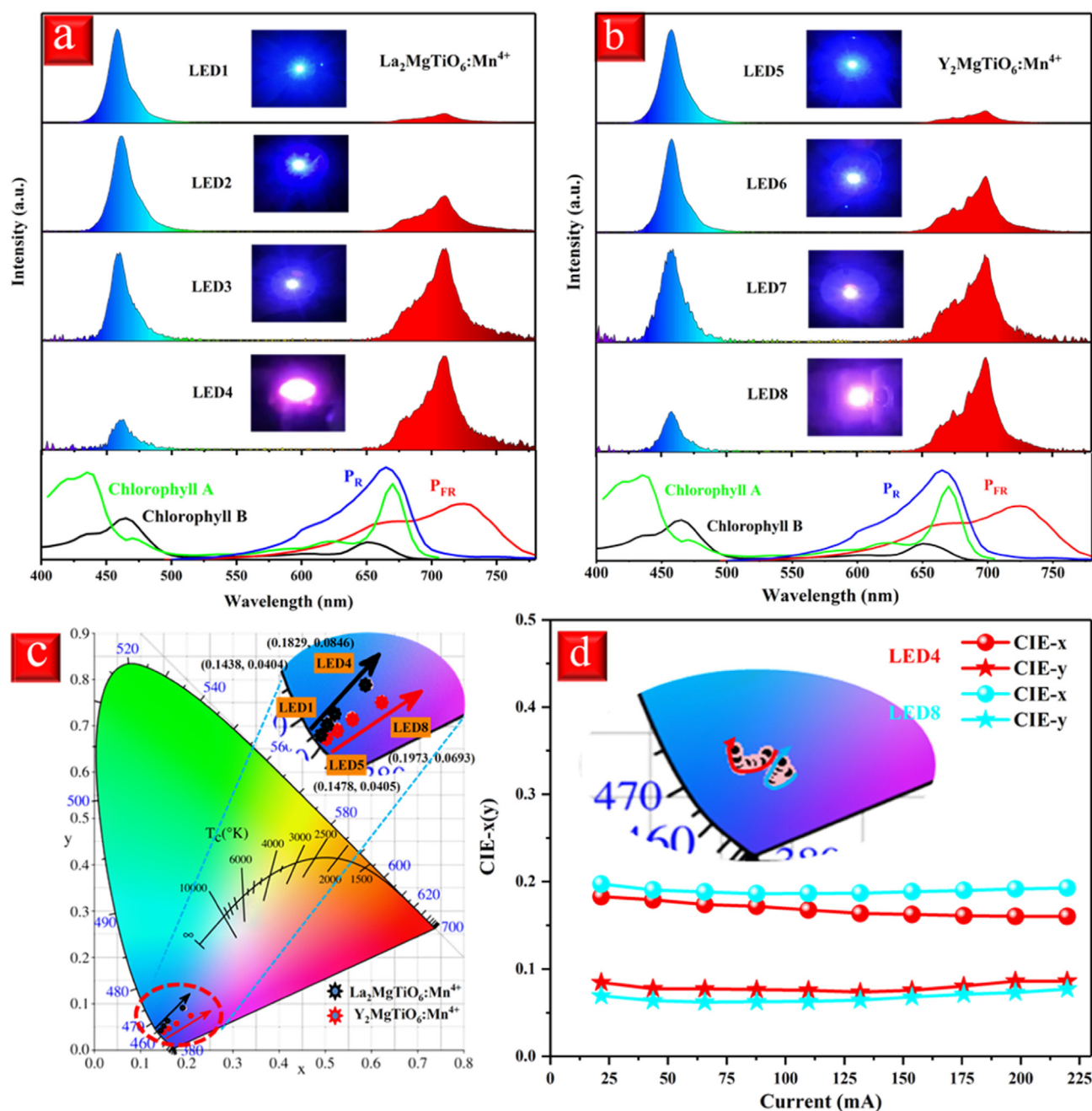
Fig. 8. (a)–(b) EL spectra of as fabricated plant growth LED1-LED8, the insets are the corresponding photographs of these LEDs; (c) CIE chromaticity diagram of LED1-LED8; the insets is the enlarged pattern; (d) the variation of CIE-x(y) under various driven currents.

refinement shows that the doping of Y^{3+} in LMT:Mn^{4+} will cause the shrinkage of the crystal lattice, resulting the peaks shift toward a higher angle. The as-prepared phosphors present bright red emission through typical $^2E \rightarrow {}^4A_2$ transition of Mn^{4+}. Its emission band shifts about 11 nm with the continuous addition of Y^{3+}, and such blue shift phenomenon could be attributed to the crystal field splitting. This shift brings the spectrum closer to the red region, making it more readily absorbed by chlorophyll A and P_R in plants. More importantly, at 150 °C, the thermal stability was significantly improved after being replaced by Y^{3+}, which increased by 26.6% and 4.5% compared to the original LMT and YMT phosphor, respectively. The as-fabricated pc-LEDs based on $La_{2-x}Y_xMgTiO_6$:Mn^{4+} phosphors have been applied in plant growth LED lighting and demonstrated potential applications. The spectroscopic properties of the Mn^{4+}-doped $La_{2-x}Y_xMgTiO_6$ are an example of advances in controlled photoluminescence tuning.

Declaration of competing interest

The authors declare that they have no known competing financial interests or personal relationships that could have appeared to influence the work reported in this paper.

Appendix A. Supplementary data

Supplementary data to this article can be found online at https://doi.org/10.1016/j.ceramint.2020.05.095.

References

[1] Z. Zhou, M. Xia, Y. Zhong, S.J. Gai, S.X. Huang, Y. Tian, X.Y. Lu, N. Zhou, $Dy^{3+}@Mn^{4+}$ co-doped $Ca_{14}Ga_{10-m}Al_{m}Zn_{6}O_{35}$ far-red emitting phosphors with high brightness and improved luminescence and energy transfer properties for plant growth LED lights, J. Mater. Chem. C 5 (2017) 8201–8210.

[2] J. Liang, L.L. Sun, B. Devakumar, S.Y. Wang, Q. Sun, H. Guo, B. Li, X.Y. Huang, Novel Mn^{4+}-activated $LiLaMgWO_{6}$ far-red emitting phosphors: high photoluminescence efficiency, good thermal stability, and potential applications in plant cultivation LEDs, RSC Adv. 8 (2018) 27144–27151.

[3] Q. Sun, S.Y. Wang, B. Devakumar, L.L. Sun, J. Liang, X.Y. Huang, Mn^{4+}-activated $BaLaMgSbO_{6}$ double-perovskite phosphor: a novel high-efficiency far-red-emitting luminescent material for indoor plant growth lighting, RSC Adv. 9 (2019) 3303–3310.

[4] Y.J. Zheng, H.M. Zhang, H.R. Zhang, Z.G. Xia, Y.L. Liu, M.S. Molokeev, B.F. Lei, Co-substitution in $Ca_{1-x}Y_{x}Al_{12-x}Mg_{x}O_{19}$ phosphors: local structure evolution, photoluminescence tuning and application for plant growth LEDs, J. Mater. Chem. C 6 (2018) 4217–4224.

[5] Z. Zhou, Y.R. Li, M. Xia, Y. Zhong, N. Zhou, H.T. Hintzen, Improved luminescence and energy-transfer properties of $Ca_{14}Al_{10}Zn_{6}O_{35}:Ti^{4+}$, Mn^{4+} deep-red-emitting phosphors with high brightness for light-emitting diode (LED) plant-growth lighting, Dalton Trans. 47 (2018) 13713–13721.

[6] Z. Zhou, Y. Zhong, M. Xia, N. Zhou, B.F. Lei, J. Wang, F.F. Wu, Tunable dual emission of $Ca_{3}Al_{4}ZnO_{10}:Bi^{3+}$, Mn^{4+} via energy transfer for indoor plant growth lighting, J. Mater. Chem. C 6 (2018) 8914–8922.

[7] J.X. Hu, T.H. Huang, Y.P. Zhang, B. Lu, H.Q. Ye, B.J. Chen, H.P. Xia, C.Y. Ji, Enhanced deep-red emission from Mn^{4+}/Mg^{2+} co-doped $CaGdAlO_{4}$ phosphors for plant cultivation, Dalton Trans. 48 (2019) 2455–2466.

[8] X.Y. Huang, H. Guo, Finding a novel highly efficient Mn^{4+}-activated $Ca_{3}La_{2}W_{2}O_{12}$ far-red emitting phosphor with excellent responsiveness to phytochrome P_{FR}: towards indoor plant cultivation application, Dyes Pigments 152 (2018) 36–42.

[9] N. Zhou, L.H. Liu, Z.P. Zhou, Y. Zhang, M.H. Li, C. Zhou, M. Xia, Z. Zhou, Engineering cation vacancies to improve the luminescence properties of $Ca_{14}Al_{10}Zn_{6}O_{35}$: Mn^{4+} phosphors for LED plant lamp, J. Am. Ceram. Soc. 103 (2019) 1798–1808.

[10] L. Shi, Y.J. Han, Z.X. Ji, Z.W. Zhang, Highly efficient and thermally stable $CaYMgSbO_{6}:Mn^{4+}$ double perovskite red phosphor for indoor plant growth, J. Mater. Sci. Mater. Electron. 30 (2019) 3107–3113.

[11] M. Xia, S.M. Gu, C. Zhou, L.H. Liu, Y. Zhong, Y.L. Zhang, Z. Zhou, Enhanced photoluminescence and energy transfer performance of $Y_{3}Al_{4}GaO_{12}:Mn^{4+}$, Dy^{3+} phosphors for plant growth LED lights, RSC Adv. 9 (2019) 9244–9252.

[12] F.F. Yao, L. Wang, Y. Lv, Y.X. Zhuang, T.L. Zhou, R.J. Xie, Composition-dependent thermal degradation of red-emitting $(Ca_{1-x}Sr_{x})AlSiN_{3}:Eu^{2+}$ phosphors for high color rendering white LEDs, J. Mater. Chem. C 6 (2018) 890–898.

[13] R.J. Xie, N. Hirosaki, T. Suehiro, F.F. Xu, M.J.C. Mitomo, A simple, efficient synthetic route to $Sr_{2}Si_{5}N_{8}:Eu^{2+}$-based red phosphors for white light-emitting diodes, Chem. Mater. 18 (2006) 5578–5583.

[14] K. Van den Eeckhout, P.F. Smet, D. Poelman, Persistent luminescence in rare-earth codoped, J. Lumin. 129 (2009) 1140–1143.

[15] J.H. Oh, H. Kang, Y.J. Eo, H.K. Park, Y.R. Do, Synthesis of narrow-band red-emitting $K_{2}SiF_{6}:Mn^{4+}$ phosphors for a deep red monochromatic LED and ultrahigh color quality warm-white LEDs, J. Mater. Chem. C 3 (2015) 607–615.

[16] W.M. Ming, H.L. Shi, M.H. Du, Doping $Y_{2}O_{3}$ with Mn^{4+} for energy-efficient lighting, J. Mater. Chem. C 6 (2018) 4171–4176.

[17] Q. Zhou, L. Dolgov, A.M. Srivastava, L. Zhou, Z.L. Wang, J.X. Shi, M.D. Dramićanin, M.G. Brik, M.M. Wu, Mn^{2+} and Mn^{4+} red phosphors: synthesis, luminescence and applications in WLEDs. A review, J. Mater. Chem. C 6 (2018) 2652–2671.

[18] W. Xu, D.Q. Chen, S. Yuan, Y. Zhou, S.C. Li, Tuning excitation and emission of Mn^{4+} emitting center in $Y_{3}Al_{5}O_{12}$ by cation substitution, Chem. Eng. J. 317 (2017) 854–861.

[19] C.S. Huang, C.L. Huang, Y.C. Liu, S.K. Lin, T.S. Chan, H.W. Tu, Ab initio-aided sensitizer design for Mn^{4+}-activated $Mg_{2}TiO_{4}$ as an ultrabright fluoride-free red-emitting phosphor, Chem. Mater. 30 (2018) 1769–1775.

[20] G.C. Xing, Y.X. Feng, M. Pan, Y. Wei, G.G. Li, P.P. Dang, S.S. Liang, M.S. Molokeev, Z.Y. Cheng, J. Lin, Photoluminescence tuning in a novel Bi^{3+}/Mn^{4+} co-doped $La_{2}ATiO_{6}:(A = Mg, Zn)$ double perovskite structure: phase transition and energy transfer, J. Mater. Chem. C 6 (2018) 13136–13147.

[21] P.Q. Cai, L. Qin, C. Chen, J. Wang, S. Bi, S.I. Kim, Y.L. Huang, H.J. Seo, Optical thermometry based on vibration sidebands in $Y_{2}MgTiO_{6}:Mn^{4+}$ double perovskite, Inorg. Chem. 57 (2018) 3073–3081.

[22] J.Q. Li, J.S. Liao, H.R. Wen, L.Y. Kong, M.H. Wang, J.L. Chen, Multiwavelength near infrared downshift and downconversion emission of Tm^{3+} in double perovskite $Y_{2}MgTiO_{6}:Mn^{4+}/Tm^{3+}$ phosphors via resonance energy transfer, J. Lumin. 213 (2019) 356–363.

[23] G.C. Xing, Y.X. Feng, Z.Y. Gao, M.X. Tao, H.Q. Wang, Y. Wei, M.S. Molokeev, G.G. Li, A novel red-emitting $La_{2}CaHfO_{6}:Mn^{4+}$ phosphor based on double perovskite structure for pc-WLEDs lighting, CrystEngComm 21 (2019) 3605–3612.

[24] J.R. Du, D. Poelman, Facile synthesis of Mn^{4+}-activated double perovskite germanate phosphors with near-infrared persistent luminescence, Nanomaterials 9 (2019) 1759–1771.

[25] M.L. Hu, C.X. Liao, L.B. Xia, W.X. You, Z.F. Li, Low temperature synthesis and photoluminescence properties of Mn^{4+}-doped $La_{2}MgTiO_{6}$ deep-red phosphor with a LiCl flux, J. Lumin. 211 (2019) 114–120.

[26] Z. Zhou, N. Zhou, M. Xia, M. Yokoyama, H.T. Hintzen, Research progress and application prospects of transition metal Mn^{4+}-activated luminescent materials, J. Mater. Chem. C 4 (2016) 9143–9161.

[27] Z.G. Xia, A. Meijerink, Ce^{3+}-Doped garnet phosphors: composition modification, luminescence properties and applications, Chem. Soc. Rev. 46 (2017) 275–299.

[28] Y. Zhong, S.J. Gai, M. Xia, S.M. Gu, Y.L. Zhang, X.B. Wu, J. Wang, N. Zhou, Z. Zhou, Enhancing quantum efficiency and tuning photoluminescence properties in far-red-emitting phosphor $Ca_{14}Ga_{10}Zn_{6}O_{35}:Mn^{4+}$ based on chemical unit engineering, Chem. Eng. J. 374 (2019) 381–391.

[29] S.S. Liang, G.G. Li, P.P. Dang, Y. Wei, H.Z. Lian, J. Lin, Cation substitution induced adjustment on lattice structure and photoluminescence properties of $Mg_{14}Ge_{5}O_{24}:Mn^{4+}$: optimized emission for w-LED and thermometry applications, Adv. Opt. Mater. 7 (2019) 1900093–1900108.

[30] J.S. Zhong, D.Q. Chen, S. Yuan, M.J. Liu, Y.J. Yuan, Y.W. Zhu, X.Y. Li, Z.G. Ji, Tunable optical properties and enhanced thermal quenching of non-rare-earth double-perovskite $(Ba_{1-x}Sr_{x})_{2}YSbO_{6}:Mn^{4+}$ red phosphors based on composition modulation, Inorg. Chem. 57 (2018) 8978–8987.

[31] Bruker AXS, TOPAS V4: General Profile and Structure Analysis Software for Powder Diffraction Data. – User's Manual, Bruker AXS, Karlsruhe, Germany, 2008.

[32] Z.W. Zhou, J.M. Zheng, R. Shi, N.M. Zhang, J.Y. Chen, R.Y. Zhang, H. Suo, E.M. Goldys, C.F. Guo, Ab initio site occupancy and far-red emission of Mn^{4+} in cubic-phase $La(MgTi)_{1/2}O_{3}$ for plant cultivation, ACS Appl. Mater. Interfaces 9 (2017) 6177–6185.

[33] T. Hu, H. Lin, Y. Cheng, Q.M. Huang, J. Xu, Y. Gao, J.M. Wang, Y.S. Wang, A highly-distorted octahedron with a C_{2v} group symmetry inducing an ultra-intense zero phonon line in Mn^{4+}-activated oxyfluoride $Na_{2}WO_{2}F_{4}$, J. Mater. Chem. C 5 (2017) 10524–10532.

[34] T. Hu, H. Lin, F.L. Lin, Y. Gao, Y. Cheng, J. Xu, Y.S. Wang, Narrow-band red-emitting $KZnF_{3}:Mn^{4+}$ fluoroperovskites: insights into electronic/vibronic transition and thermal quenching behavior, J. Mater. Chem. C 6 (2018) 10845–10854.

[35] M. Zhao, H.X. Liao, L.X. Ning, Q.Y. Zhang, Q.L. Liu, Z.G. Xia, Next-generation narrow-band green-emitting $RbLi(Li_{3}SiO_{4})_{2}:Eu^{2+}$ phosphor for backlight display application, Adv. Mater. 30 (2018) 1802489–1802495.

[36] M.H. Fang, S. Mahlik, A. Lazarowska, M. Grinberg, M.S. Molokeev, H.S. Sheu, J.F. Lee, R.S. Liu, Structural evolution and effect of the neighboring cation on the photoluminescence of $Sr(LiAl_{3})_{1-x}(SiMg_{3})_{x}N_{4}:Eu^{2+}$ phosphors, Angew. Chem. Int. Ed. 58 (2019) 7767–7772.

[37] H.X. Liao, M. Zhao, Y.Y. Zhou, M.S. Molokeev, Q.L. Liu, Q.Y. Zhang, Z.G. Xia, Polyhedron transformation toward stable narrow-band green phosphors for wide-color-gamut liquid crystal display, Adv. Funct. Mater. 29 (2019) 1901988–1901994.

[38] R.P. Cao, X.F. Ceng, J.J. Huang, X.W. Xia, S.L. Guo, J.W. Fu, A double-perovskite $Sr_{2}ZnWO_{6}:Mn^{4+}$ deep red phosphor: synthesis and luminescence properties, Ceram. Int. 42 (2016) 16817–16821.

[39] J.S. Liao, Q. Wang, H.R. Wen, H.L. Yuan, S.J. Liu, J.X. Fu, B. Qiu, First observation of mutual energy transfer of $Mn^{4+}-Er^{3+}$ via different excitation in $Gd_{2}ZnTiO_{6}:Mn^{4+}/Er^{3+}$ phosphors, J. Mater. Chem. C 5 (2017) 9098–9105.

[40] L.L. Sun, J. Liang, B. Devakumar, Q. Sun, S.Y. Wang, B. Li, X.Y. Huang, Preparation, characterization, and luminescence properties of double perovskite $SrLaMgSbO_{6}:Mn^{4+}$ far-red emitting phosphors for indoor plant growth lighting, RSC Adv. 8 (2018) 35187–35194.